Carbohydrate Polymers 305 (2023) 120536

Contents lists available at ScienceDirect

Carbohydrate Polymers

journal homepage: www.elsevier.com/locate/carbpol

ZnO microrods sandwiched between layered CNF matrix: Fabrication, stress transfer, and mechanical properties

Ying Gao [a,b], Bin Chen [b], Marcus Vinícius Tavares da Costa [b], Hongqi Dai [a], Farsa Ram [b,*], Yuanyuan Li [b,*]

[a] Co-Innovation Center of Efficient Processing and Utilization of Forest Resources, Nanjing Forestry University, Nanjing 210037, China
[b] Wallenberg Wood Science Center, Department of Fibre and Polymer Technology, KTH Royal Institute of Technology, SE-10044 Stockholm, Sweden

ARTICLE INFO

Keywords:
Cellulose nanofibrils
Zinc oxide
Layered composites
Stress transfer
Sensor

ABSTRACT

Functional metal oxide particles are often added to the polymers to prepare flexible functional polymer composites with adequate mechanical properties. ZnO and cellulose nanofibrils (CNF) outstand among these metal oxides and the polymer matrices respectively due to their various advantages. Herein, we *in situ* prepare ZnO microrods in the presence of CNF, which resultes in a layered composite structure. The ZnO microrods are sandwiched between the CNF layers and strongly bind to highly charged CNF, which provides a better stress transfer during mechanical activity. Digital image correction (DIC) and finite element analysis-based computational homogenization methods are used to investigate the relationship between mechanical properties and composite structure, and the stress transfer to the ZnO microrods. Full-field strain measurements in DIC reveal that the *in situ* ZnO microrods preparation leads to their homogenous distribution in the CNF matrix unlike other methods, which require external means such as ultrasonication. The computational homogenization technique provides a fairly good insight into the stress transfer between constituents in microstructure as well as a good prediction of macroscopic mechanical properties, which otherwise, would be challenging to be assessed by any ordinary mechanical testing in the layered composites. Finally, we also demonstrate that these composites could be used as physiological motion sensors for human health monitoring.

1. Introduction

Metal oxide particles are widely used in many fields for biological, technological, energy, and environmental applications due to their unique functional properties. Owing to their high density and brittle nature they are often added to the polymer matrix to prepare flexible polymer composites (Sarkar et al., 2012). This approach is elegant, and renders the functional materials embedded with metal oxide particles in the forms of films, fibers, gels, and foams (Gullapalli et al., 2010; Ltaief et al., 2021; Ram et al., 2021; Shifrina et al., 2020), and so on. However, metal oxide particles are often prepared using energy-intensive multi-step processes and sometimes require additional high-temperature sintering (Siponkoski et al., 2022). For example, lead zirconate titanate (PZT) (Chen et al., 2021), lead magnesium niobate-lead titanate (PMN-PT) (Wang et al., 2021a, 2021b), or lead-free metal oxides particles such as sodium niobate ($NaNbO_3$) (Li et al., 2021a), barium titanate ($BaTiO_3$) (Sada et al., 2021), and ZnO (Serrano et al., 2020). ZnO in this regard is interesting and can be easily prepared in one step or at lower temperatures (Gerbreders et al., 2020; Ram et al., 2022). The easier synthesis methods also offer tunability in the particle morphology by variation of simple parameters such as concentration of Zn salt, temperature, pH, etc. (Wang, 2004). In addition to the ease of preparation, ZnO also provides multifunctional properties such as ultra-violet (UV)-shielding, antibacterial, photocatalytic, piezoelectric, hydrophobic, etc., which are unique to other metal oxide particles (Wang, 2004; Wang et al., 2021a, 2021b). Additionally, it also offers several other advantages over its other counterparts including lower cost, and relatively environmentally friendliness (Gao et al., 2007; Gullapalli et al., 2010; Liao et al., 2014) are a few to name.

Preparing the polymer composite with desired functional and mechanical properties require careful selection of polymer matrix, where ZnO particles with a few polymers may result in poor interface compatibility (Wang et al., 2021a, 2021b). On the other side, CNF act as a promising polymer matrix for ZnO due to the high binding affinity of

* Corresponding authors.
E-mail addresses: farsa@kth.se (F. Ram), yua@kth.se (Y. Li).

https://doi.org/10.1016/j.carbpol.2022.120536
Received 11 October 2022; Received in revised form 28 December 2022; Accepted 31 December 2022
Available online 6 January 2023

Fig. 1. The preparation steps of sandwich structured ZnO/CNF composite films.

the Zn cation to hydroxyl/carboxyl functionalities of CNF (Lizundia et al., 2016). ZnO/CNF composites can be prepared using various methods, for example, dispersing ZnO nanoparticles in a casting solution (Lizundia et al., 2016) or growing ZnO particles on a cellulosic substrate (Gullapalli et al., 2010; Zhang et al., 2014). The former is a probably simpler method but usually led to inhomogeneous ZnO distribution in the composites, and requires additional dispersion techniques such as ultrasonication to uniformly disperse ZnO particles. The latter usually requires dipping of the substrate in ZnO colloidal solution and drying, which leads to substrate shrinkage. Additionally, a hydrothermal growth step is followed to achieve higher ZnO content. *In situ*, synthesis of ZnO in presence of CNF not only reduces the number of steps to prepare the composites but also ensures a better interface between ZnO particles and CNF. For example, Rabani et al. *in situ* prepared ZnO nanoparticles (NPs) in presence of CNF, and prepared composites were utilized for UV radiation blocking and photocatalytic applications (Rabani et al., 2021). Similarly, Dehghani et al. *in situ* prepared ZnO and used ZnO/CNF for waste-water treatment by demonstrating photocatalytic degradation of methylene blue dye (Dehghani et al., 2020). However, these reports were limited to the ZnO spherical nanostructures morphology. Additionally, little to no attention was paid to the mechanical properties, which is an important parameter for designing durable and functional materials. ZnO rods are superior to spherical particles in terms of mechanical reinforcement and their functional reactivity e.g. photocatalytic activity and piezoelectric property (Ong et al., 2018). Li et al. reported the in-situ synthesis of ZnO microrods in presence of ultrasonicated cellulose fibers and embedded them into a natural rubber matrix. However, the study does not report the mechanical properties of ZnO/CNF composites (Li et al., 2019).

In this work, ZnO/CNF composites were fabricated by *in situ* synthesis of ZnO microrods in presence of CNF, followed by filtration and drying (Fig. 1). In the resultant layered structure, ZnO microrods were sandwiched between CNF layers. We hypothesized that the CNF coating on ZnO rods will not only results in better interface compatibility and mechanical properties but also it can serve as a stress transfer pathway to the ZnO rods. We examined the mechanical properties of these ZnO/CNF composites having different ZnO content. Further, to establish the relationship between mechanical properties and composite structure, or interface compatibility between CNF and ZnO and the stress transfer mechanism; DIC and finite element-based computational homogenization techniques were utilized. DIC is a non-contact, full-field, and easy-to-implement experimental mechanics method. It accurately retrieves the strain fields of the sample surface by processing the images at varied states (Wu et al., 2016). DIC has been widely used in evaluating the complicated deformation behavior of various films, such as adaptive nanocomposites using cellulose nanocrystal (CNC) and poly butyl methacrylate (Ding et al., 2019), gradient bioinspired nanocomposites based on CNF (Wang et al., 2016), etc. Additionally, the computational homogenization technique was employed (Karakoç et al., 2021; Yvonnet, 2019), to study the stress distribution in the ZnO microrods in the layered CNF, which otherwise, would be challenging to be assessed by any ordinary mechanical testing. This provides a fairly good insight into the stress transfer between constituents in microstructure as well as a good prediction of macroscopic mechanical properties (Mirkhalaf et al., 2020). These studies are unique for *in situ* prepared ZnO/CNF composites, whereas previous studies are only focused on targeted applications or occasionally studies mechanical properties. Finally, we also demonstrated the utilization of these ZnO/CNF composites as physiological motion sensors, which could be used for human health monitoring.

2. Experiment section

2.1. Materials

Softwood bleached pulp (derived for pine) from the sulfite process was supplied by Nordic Paper Säffle AB (Säffle, Sweden) with 14 wt% hemicellulose and <1 % lignin. 2,2,6,6-tetramethylpiperidine-1-oxyl (TEMPO), sodium bromide (NaBr), sodium hydroxide (NaOH), sodium chlorite ($NaClO_2$), sodium acetate (CH_3COONa), zinc nitrate hexahydrate ($Zn(NO_3)_2{\cdot}6H_2O$), and hexamethylenetetramine (HMTA) were purchased from Sigma-Aldrich, Sweden. 14 wt% sodium hypochlorite (NaClO) was purchased from VWR International. All the chemicals were used as received.

2.2. Preparation of CNF

CNF was prepared using the previous protocol (Kobayashi et al., 2014). Briefly, the softwood pulp (1 g dry weight) was suspended in 100

Table 1
Composition of different weight ratio composite film.

Amount added	CNF	ZC1	ZC2	ZC3
CNF (g)	0.5300	0.2500	0.1970	0.1860
0.4M $Zn(NO_3)_2$ (mL)	/	5.3	7.5	9

mL distilled water and mixed with 0.016 g TEMPO and 0.1 g NaBr. Thereafter, 2.1 mL of a 1.8 M NaClO solution was added dropwise under stirring (the available chlorine is 14 %). The pH of the mixture was maintained at ≈10 by adding 1 M NaOH during the process. The reaction was stopped after 1 h and the pulp was washed with distilled water. Further, oxidization treatment of the pulp was conducted with 1 % w/v $NaClO_2$ in 100 mL acetate buffer at pH 4.8 for 48 h. After the oxidation pre-treatment, the fibers were thoroughly washed with distilled water and disintegrated using a Microfluidizer (M-110EH, Microfluidics Ind., USA) by passing one time through a pair of 400 μm and 200 μm microchannels, followed by a pair of 200 μm and 100 μm microchannels to obtain a CNF viscous gel of around 1 wt%. The CNF has a hemicellulose content of 4 wt% with negligible residual lignin content.

2.3. Preparation of ZnO/CNF (ZC) composite

The growth of ZnO microrods with CNF was achieved using hydrothermal synthesis. The CNF gel was dispersed in deionized water using ULTRA-TURRAX mixer (IKA T25, Germany) at 12,000 rpm for 45 s. To this suspension, equimolar solutions of $Zn(NO_3)_2{\cdot}6H_2O$ (0.4 M) and HMTA (0.4 M) in different volumes were added and heated at 95 °C for 2 h under constant stirring. According to the added volume from low to high, the samples were labeled as ZC1, ZC2, and ZC3 (see Table 1).

The casting dispersion was collected on the filter paper (pore diameter = 0.1 μm) by vacuum filtration. After infiltration, the wet composite cakes were dried in a Rapid Köthen sheet-forming equipment (Frank-PTI GmbH, Germany) at 90 °C under 0.8 KPa for 10 min. An overview of the whole process is illustrated in Fig. 1.

2.4. Characterization

2.4.1. Field-emission scanning electron microscopy (FE-SEM)

SEM images were taken using a FE-SEM (Hitachi S-4800, Japan) operating at an accelerating voltage of 1 kV. Pt/Pd coating was sputtered on the samples for 20 s before imaging.

2.4.2. Atomic force microscopy (AFM)

A Bruker Multimode 8 was used for AFM. The cantilevers had a nominal tip radius of 2 nm and a spring constant of 0.4 N/m, the AFM was operated in the ScanAsyst mode. Before the test, silicon wafers were thoroughly cleaned, plasma treated for 2 min, and then submerged in a 0.1 wt% polyethyleneimine solution for 10 min. It was then rinsed with DI water, and allowed to dry before being submerged in CNF dispersion (0.1 g/L) for 10 min.

2.4.3. Thermogravimetric analysis (TGA)

TGA was performed to measure the ZnO loading in the ZnO/CNF composite film at a heating rate of 10 °C/min from room temperature to 800 °C under O_2 flow of 50 mL/min. The measurements were made using the Q500 (TA Instruments, USA), which has a weight sensitivity of ±0.1 μg, a temperature sensitivity of ±0.01 °C, a dynamic baseline drift of ±50 μg determined by the manufacturer using empty alumina pans at a temperature ramp of 20 °C/min with no baseline correction.

2.4.4. X-ray diffraction (XRD)

X-ray diffraction allows the structural information of the materials to be obtained. XRD was performed in a powder diffractometer (Thermo Fisher Scientific ARL X'TRA powder diffractometer) having CuKα radiation (λ = 1.54060 Å) at 40 mA and 45 kV. Scans were obtained from 5 to 70° 2θ in steps of 0.02° for 1 s per step. The average grain size of ZnO microrods was calculated using the characteristic peaks (100), (002), and (101) by Scherrer's equation (Karlsson et al., 2018):

$$D = \frac{K\lambda}{\beta cos\theta}$$

where D is the average diameter of ZnO nanoparticles, λ represents the X-ray wavelength (0.154 nm), K refers to the Scherrer constant (0.89), β is the full width of the peak at half maximum (FWHM), and θ represents the Bragg diffraction angle.

2.4.5. Fourier-transform infrared (FTIR) spectroscopy

FTIR spectra were obtained at 16 scans and a resolution of 4 cm^{-1} in transmission mode with a Spectrum 100 FT-IR Spectrometer (Perkin Elmer, UK). The scan range was fixed between 400 and 4000 cm^{-1}.

2.4.6. Mechanical properties

Tensile tests were performed using an Instron 5944, which is equipped with a 500 N load cell and a video extensometer. All the samples were cut into rectangular strips along the desired direction (longitudinal or transverse) and conditioned at a relative humidity of 50 % and 23 °C for a minimum of 3 days. Samples had a width of 5 mm, the gauge length was 25 mm, and the strain rate was 10 % per minute. A minimum of five specimens were tested for each type of sample.

2.4.7. Zeta potential

The Zetasizer ZEN3600 instrument from Malvern Instruments was utilized for charge determination of CNF dispersions in water with a concentration of 0.1 wt% at pH = 6.6. Three measurements were made for each sample. Typically, a zeta potential of greater than or equal to ±61 mV denotes exceptional stability, between ±40 to ±60 mV, good stability, and between ±30 to ±40 mV, moderate stability (Kumar & Dixit, 2017).

2.4.8. Porosity and measured density

All the samples were cut into 1 × 1 cm^2 and dried in a vacuum oven at 90 °C for 24 h for measuring the density. The porosity of all the samples is calculated by the following equation:

$$P_T = 1 - \frac{\rho_M}{\rho_S}$$

where P_T is the total porosity, ρ_M is the measured bulk density (g/cm^3), ρ_S is the theoretical composite density (g/cm^3), ρ_{ZnO} is 5.6 g/cm^3, ρ_{CNF} is 1.6 g/cm^3.

2.4.9. Digital image correlation (DIC)

The samples were preprocessed by applying black random speckle patterns on one surface. A Basler acA4096-30 μm camera with a resolution of 4096×2168 pixels was perpendicularly fixed in front of the sample to record the image sequence during the tensile tests. A telecentric lens that can alleviate the possible virtual strain caused by out-of-plane displacement was mounted on the camera. A monochrome blue light source was used to light the sample surface, while polarizers were fixed on the lens and the light source to prevent the specular reflection on the sample. Carefully adjusting the lens, high contrast and sharp images could be observed through the camera. The images were captured at a frame rate of 1 frame per second. The image sequences were then processed using VIC-2D 6 (Correlated Solutions, Inc., USA). A grid of calculation points with a step size of 11 pixels was selected on the image at the initial state and then matched to the other images with a subset size of 51×51 pixels. The strain window size was set to 7×7 points.

2.4.10. Computational homogenization

A standard finite-element-based simulation was performed for

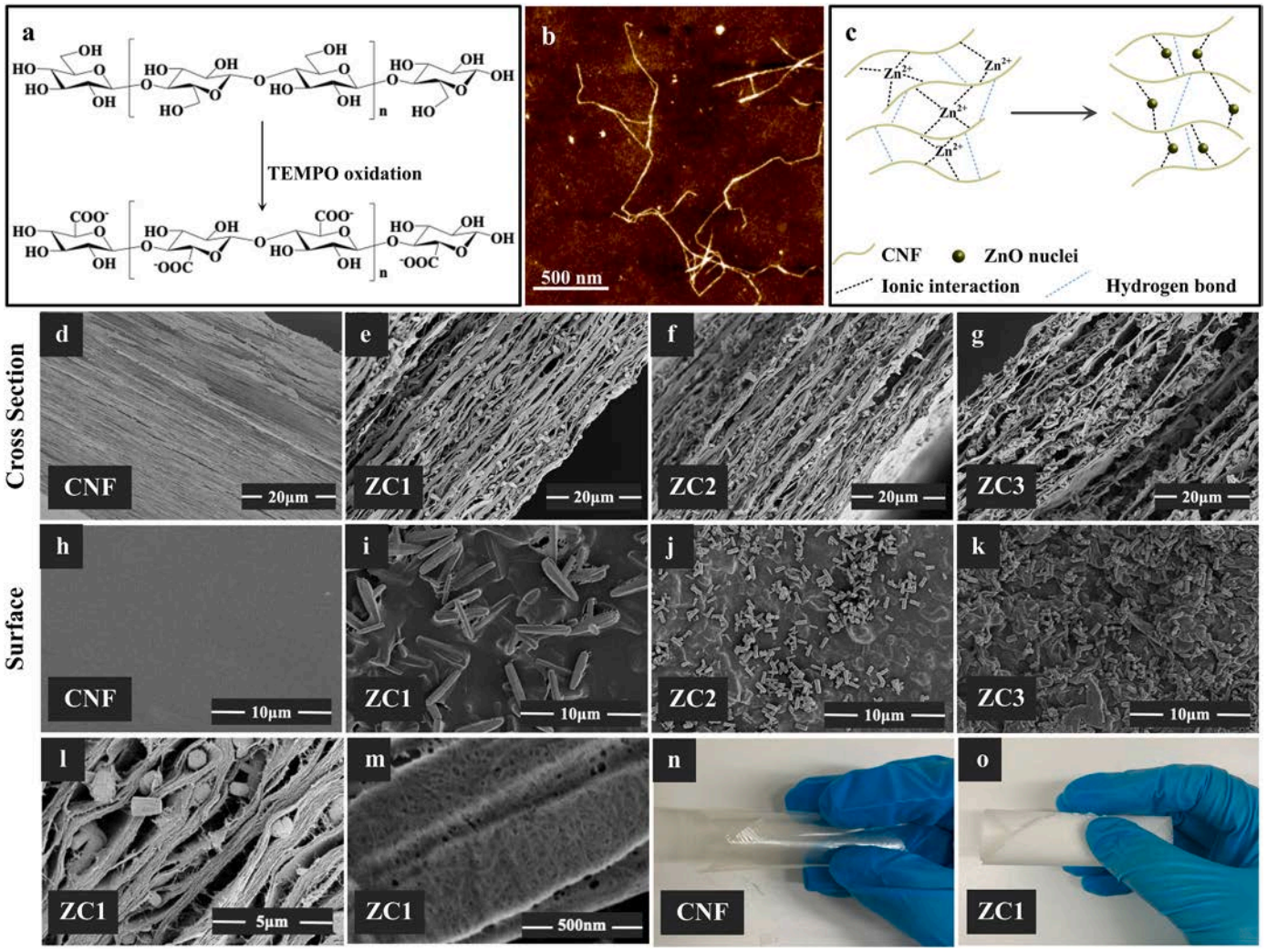

Fig. 2. (a) Schematic illustration of the high charge introduction in CNF during the TEMPO oxidation. (b) AFM image of CNF. (c) Proposed mechanism of ZnO formation in presence of CNF. (d–g) are the cross-section SEM images of CNF and ZC films; (h-k) are the surface SEM images of CNF and ZC films; (l) is the high-resolution cross-section SEM image of ZC1; (m) is the high-resolution surface SEM image of ZC1; (n–o) are the photos of CNF and ZC1 films showing their flexibility.

computational homogenization to verify the composite modulus along the microrods (E_L) and the stress distribution in the composite material. The reference sample was the ZC1 sample, where the microrods are relatively more oriented and distributed as revealed in the microscopy images. The material models are orthotropic linear elastic with elastic modulus along the rods of 116 GPa and in the radial direction of 65 GPa (Yan et al., 2010). The Poisson ratio of the rods is assumed to be 0.33 (Yan et al., 2010) and the shear moduli are simply calculated from $G = E/(1+\nu)$ for a corresponding direction. The average strain approach of the solid mechanics' module in COMSOL Multiphysics was used by prescribing 0.2 % tensile strain in the entire geometry while having periodic boundary conditions on the outer surfaces. This amount of strain corresponds to the elastic limit in tensile testing observed in the experiments. Higher-order quadrilateral elements were used in the whole geometry with shared nodes at the interfaces between the materials. The composite modulus (E_L) was then estimated by dividing the average stress in the entire geometry by the prescribed strain.

2.4.11. Physiological motion sensors

Physiological motion sensors were fabricated in the following steps: 1) Cutting the CNF and ZnO/CNF films in the desired size (5×1 cm^2), 2) followed by silver paste coating on both sides and then drying in the oven at 80 °C for 2 h, and 3) by attaching the copper electrodes on the corner to solder a set of copper wires and finally encapsulating in a thin layer of poly(dimethylsiloxane). The sensors were mounted on the wrist, finger, elbow, or knee with the help of tapes. The signals generated from the sensors by physiological movements were then measured using Keithley's DMM 7510. All the samples were tested over a hundred cycles.

3. Results and discussion

3.1. Morphological analysis of CNF and ZC films

The CNF showed a high zeta potential of -71.37 ± 8.29 mV, and the charge density of 1000 μequiv/g after TEMPO oxidation (Fig. 2a). The CNF diameter is 2–3 nm with a typical length ranging from 1 to 2 μm with some kinks (Figs. 2b and S1). The ZnO microrods were *in situ* synthesized in one step in the presence of CNF, where highly charged CNF enhanced the Zn^{2+} binding for initiating the ZnO particle growth (Fig. 2c). The pure CNF film surface appeared relatively smooth and had an obvious layered structure due to the hydrogen bonding interactions between CNF (Fig. 2d, h) (Nie et al., 2019). The interaction between CNF and Zn^{2+} or ZnO also led to the uniform coating of the CNF on the ZnO microrods. ZC films showed higher porosity compared with CNF films (Fig. 2e–g). ZnO microrods were near evenly distributed within CNF

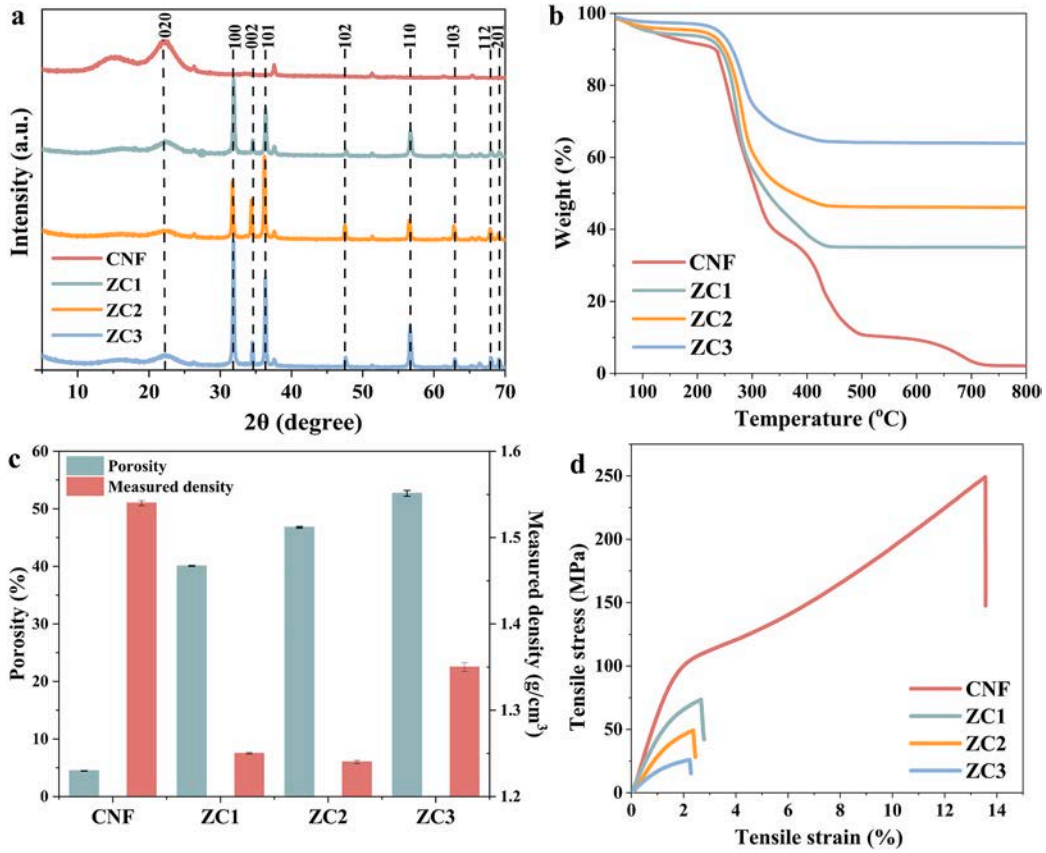

Fig. 3. (a) Powder XRD patterns of CNF and ZC films with different ZnO content; (b) TGA curves (in presence of O_2) of CNF and ZC with different ZnO content; (c) The porosity and measured density of CNF and ZC films; (d) Mechanical properties of CNF and ZC films with different ZnO content.

layers having an individual thickness of around 0.5 μm. On the surface, ZnO microrods are randomly oriented. The ZnO microrods ratio of length/diameter becomes smaller with the increase of Zn^{2+} concentration. The microrods in ZC1 have diameters around 0.5–0.8 μm and lengths in the range of 3–5 μm, while the microrods in ZC2 and ZC3 have diameters in the range of 0.4–0.5 μm and lengths around 1 μm (Fig. 2i-k). When the zinc salt solution was added to the CNF suspension, the Zn^{2+} ions were captured by the polar carboxyl or hydroxyl of highly charged CNF. Having strong electrostatic interactions with the electron-rich oxygen atoms, Zn^{2+} can turn into ZnO nuclei (Fig. 2c) (Hoogendoorn et al., 2022; Li et al., 2021b). This effect is stronger in highly charged CNF compared to mechanically fibrillated low-charged CNF, due to enhanced interaction provided by the chelation ability of the carboxyl functionalities. The availability of carboxyl/hydroxyl charge controls the nucleation density of ZnO, which affects the dimensions of ZnO. At a lower CNF concentration, increased Zn^{2+} concentration leads to more availability of Zn^{2+} for interaction hence the more nucleation of ZnO. And at the higher nucleation density, the ZnO microrods dimensions are reduced due to increased competitive growth. This suggests that the ratio of CNF to Zn ion did not directly affect the shape of ZnO but slightly changed their dimensions. At the same time, the CNF covered the ZnO microrods uniformly, which could ensure the internal stress transfer to the ZnO microrods and contributes to the mechanical properties of the composites.

The high-resolution SEM images of ZC1 showed that the ZnO microrods are embedded within several interconnected layers of CNF (Fig. 2l), and CNF also covered the whole ZnO surface (Fig. 2m). The CNF layer thickness decreased with increased Zn^{2+} concentration, which can be attributed to the reduced hydrogen bonding interactions and increased ionic interaction in the presence of Zn^{2+}. At lower concentrations, the ZnO microrods have a higher aspect ratio which locks their orientation in-plane. At higher Zn^{2+} concentrations, the aspect ratio of ZnO microrods decreased and microrods can also arrange themselves out of the plane, which leads to an increase in interlayer spacing. CNF film appeared to be a transparent thin film (Fig. 2n), whereas the ZC film showed white color due to the embedded ZnO microrods (Fig. 2o) and both films exhibited flexibility.

3.2. Structural characterizations and mechanical properties of CNF and ZC films

Fig. 3a shows the XRD patterns of CNF and ZC composites with different ZnO contents. The XRD patterns indicate the formation of ZnO microrods with Wurtzite-type crystalline structure (Wurtzite-type, JCPDS Card No. 75-0576) at 2θ value of 31.7° (100), 34.6° (002), 36.2° (101), 47.5° (102), 56.6° (110), 62.8° (103), 67.9° (112) and 69.1° (201). An additional broad peak at 22.1° (020) corresponds to the CNF with cellulose I crystal structure. The average ZnO crystallite size was estimated using Scherrer's formula and found to be 31.40 nm, 34.59 nm, and 35.99 nm corresponding to ZC1, ZC2, and ZC3. This suggests that the variation of ZnO microrods volume fraction (originally varying the Zn ion concentration) also increased their crystallite size without altering their Wurtzite crystalline structure. The ZnO contents of different ZC films were determined by TGA running under O_2 (Fig. 3b). ZnO has high thermal stability up to 800 °C (Park et al., 2019). However, CNF started to decomposite at approximately 240 °C. During further heating, it burnt off leaving only ZnO. The ZnO contents of ZC1, ZC2, and ZC3 were found to be 32.9 wt%, 44.0 wt%, and 61.8 wt%.

With the increased ZnO content, the CNF layers thickness reduced from 2 μm to 0.5 μm, and increased the CNF layer spacing from 1 μm to 5 μm. This increased the porosity of the composites, which in turn resulted in reduced mechanical properties of ZC2 and ZC3 composites

Table 2
In-situ cellulose/ZnO materials and their mechanical properties.

Base material	ZnO morphology	ZnO content (wt%)	Tensile strength (MPa)	Modulus (GPa)	Reference
Cellulose	Spheroid	14.9	44.1	3.2	(Fu et al., 2017)
Bacterial cellulose	Spheroid	5	29.7	2.4	(Luo et al., 2020)
Bacterial cellulose	Spheroid	5	21.9	1.3	(Ul-Islam et al., 2014)
Cellulose fibers	Rod	16.5	/	/	(Li et al., 2019)
CNF	Sheet-like	48	/	/	(Dehghani et al., 2020)
CNF	Rod	32.9	73.5	4.8	This work

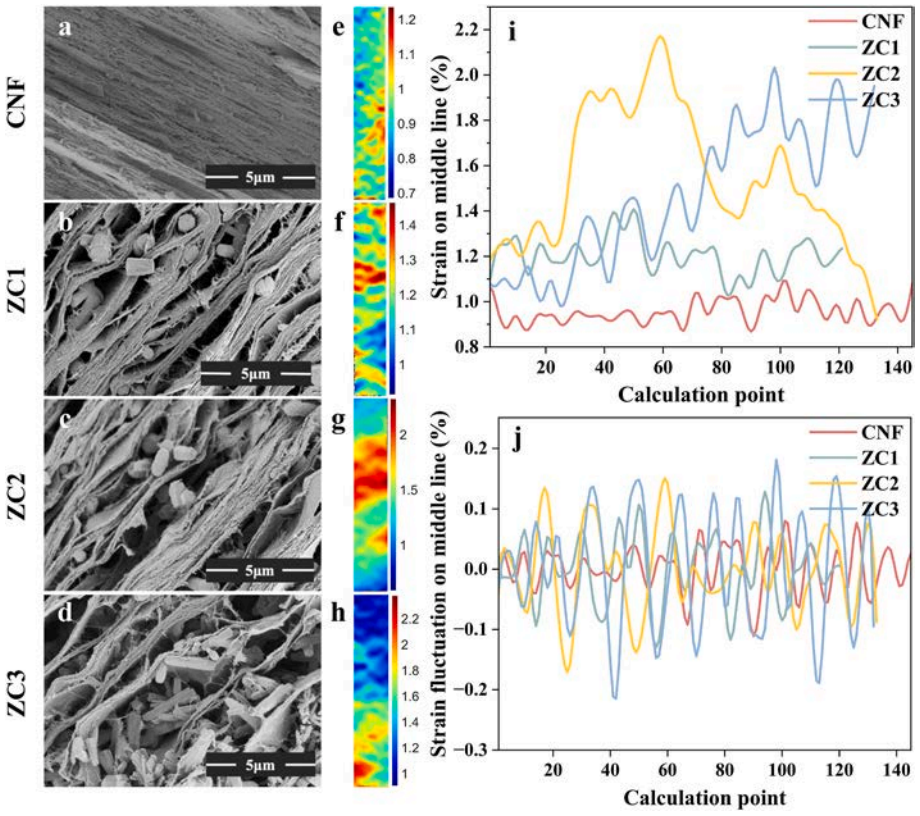

Fig. 4. Digital image correlation (DIC) of CNF and different ZC samples and the SEM images of cross-sections after DIC tensile strain test. All the DIC images are the tensile strain map. (a–d) are the images of CNF, ZC1, ZC2, and ZC3 samples. (e–h) are the strain maps (unit: %) of CNF, ZC1, ZC2, and ZC3 samples. (i) The tensile strain distribution on the central lines of the samples at 100 s. (j) The strain noise on the central lines of the samples at 100 s by removing the systematical strain components through curve fitting.

(Fig. 3c). With increased porosity and increased ZnO microrods content, the measured density decreased from CNF to ZC composites. Within ZC composites, with the increased ZnO content, the density of the composites also increased due to the higher density of ZnO. However, the measured density of ZC2 is slightly lower than ZC1 due to the increased porosity of ZC2. All specific data are shown in Supporting Table 2.

Fig. 3d shows the stress−strain curves of CNF and ZC films. CNF had a tensile strength (σ_b) and Young's modulus (E) of 248.61 MPa and 6.79 GPa, respectively. The high strain value of CNF film is mainly because of the high aspect ratio of CNF (Figs. 2b and S1). Adding ZnO microrods led to a significant decrease in both σ_b and E and the values decreased with increased ZnO loading. The Young's modulus of ZC1, ZC2, and ZC3 was 4.76 GPa, 3.24 GPa, and 2.04 GPa respectively, while σ_b values were found to be 73.52 MPa, 49.24 MPa, and 25.94 MPa, respectively. The strong hydrogen bonding between CNF fibrils improves the mechanical properties in vacuum-filtered CNF films (Zhang et al., 2019). At lower concentrations, ZnO acts as a reinforcing filler and enhances the mechanical properties of composites. However, at higher ZnO concentrations, the brittleness from ZnO reduces the mechanical properties of composites. At the high ZnO concentration of 32.9 wt%, the ZC1 composites exhibited higher tensile strength and Young's modulus compared to the previous reports (Table 2). This can be attributed to the enhanced secondary interactions between CNF and ZnO, where CNF strongly binds and coats the ZnO microrods leading to increased interfacial compatibility between CNF and ZnO, which prevents abrupt mechanical failure. Thus, the CNF coating on ZnO microrods helps in enhancing mechanical properties of the composite.

3.3. Digital image correlation (DIC) studies of CNF and ZC films

To evaluate the effect of the material microstructure, a non-contact image-based DIC technique (Pan et al., 2009; Schreier et al., 2009) for full-field strain measurement was employed. The mechanical performances of the samples subjected to uniaxial tensile load are evaluated by measuring their strain distribution on the specimen surfaces. Fig. 4a–d are the cross-sectional SEM images of the samples showing the clear layered structures with ZnO sandwiched in between the CNF layers. The tensile strain maps on the sample surface at 100 s are presented in Fig. 4 (e–h) and in the supplementary video S1. Inhomogeneous strain distribution is shown on these samples. To better evaluate and compare the strain distribution, the strain distributions along the vertical central line of the samples at 100 s are presented in Fig. 4(i). Obvious global strain variation exists along the longitudinal direction, see Fig. 4(e–h) and (i), which may be resulted from the ZnO accumulation in the structure and imperfect sample preparation and loading. In Fig. 4(j), the global strain inhomogeneity along the central line is removed by fitting the curves

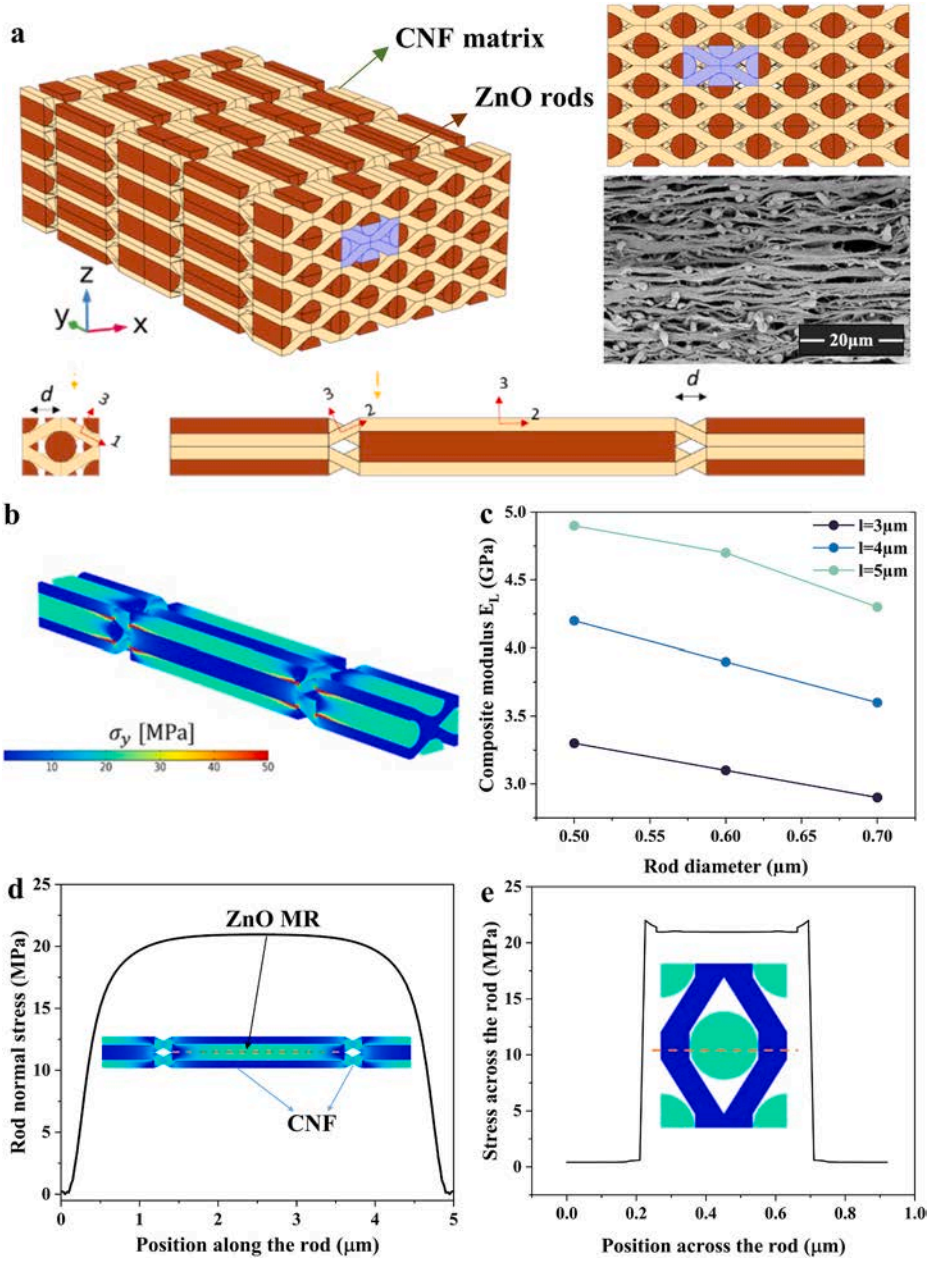

Fig. 5. (a) 3D model based on the microstructure of ZC1 samples from microscopy images. (b) Parametric study showing the stress transfer in the ZnO rod embedded in CNF matrix. (c) Composite modulus with the variation in the diameter and length of the rod. (d–e) Shows the normal stress distribution along and across the rod with its stress fields in the y-direction (tensile).

with 10th order polynomial function and then removing the fitted components. In this way, the obtained curves can well present the strain inhomogeneity resulting from the sample itself by alleviating the influence of imperfect sample preparation and loading during the tensile test. This random fluctuation (Fig. 4j) indicates that even if ZnO is well distributed in the materials, it will also inevitably lead to more inhomogeneous deformation of the sample. The random strain fluctuation is the least for CNF, which increases with the ZnO loading increase. The possible reason for this is the larger aggregations in the composites with higher ZnO loading (Fig. 4a–d). This supports the better mechanical performance of ZC1 obtained from the tensile test.

3.4. Predictions of composite modulus and stress distribution of ZnO/CNF films

To further understand the stress transfer in the ZnO/CNF composites, a finite-element-based simulation model was built. Fig. 5a shows the model structure based on ZC1 samples where the rods are relatively more oriented and distributed from microscopy images. Note that the microscopy images are from post-mortem fracture surfaces so the model geometry is not identical to the images (e.g. some rods are not aligned and some rod agglomerations are seen), however, the fractography in Fig. S1 indicates that there are many aligned rods and we assume those are from undamaged structure. The proposed composite structure is also periodic with even spacing between the rods to facilitate the computation performance. Fig. 5b shows the simulated stress transfer in a unit cell of ZC1 (detailed information in the experimental section), where ZnO microrods are embedded in the CNF matrix, where CNF act as a stress transfer bridge to the ZnO rod. The 3D periodic geometry can be seen in Fig. 5b where dimension d, which is set at 0.5 μm from SEM images, controls the porosity. The diameter of the rods varies from 0.5 to 0.8 μm and its length from 3 to 5 μm by also examining the SEM images

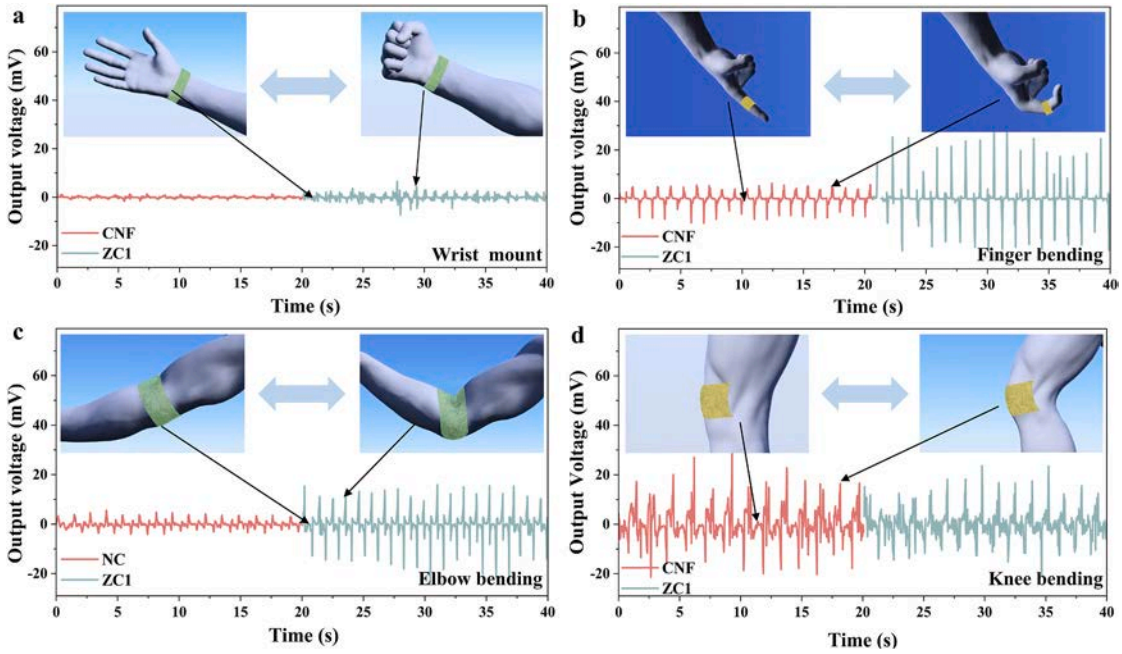

Fig. 6. Sensing of human physiological motions using CNF and ZnO/CNF-based flexible sensors. The schematics show the idle and the action state of physiological motions, (a) under fist clenching (mounted on the wrist) (b) finger bending, (c) elbow bending, and (d) knee bending, and their corresponding piezoelectric voltage output signals from CNF and ZC1 are shown below.

in this work. The properties of the CNF matrix follow its complex geometry and are oriented in the 1-2-3 coordinate system shown at the bottom of Fig. 5b. The in-plane moduli are $E_1 = E_2 = 6$ GPa from the tensile testing of neat CNF. The modulus in the 3-direction is $E_3 = 2$ GPa estimated from reference (Song et al., 2021) by comparing the ratio of moduli in different directions. The Poisson ratios are $\nu_{12} = 0.1$, $\nu_{23} = \nu_{13} = 0.33$ (Nakamura et al., 2004; Song et al., 2021) and the shear moduli are 2.5 GPa (Molnár et al., 2018). Fig. 5c shows a parametric simulation varying the size of the rods for E_L. By increasing the diameter of the rods, the composite modulus decreases given the interface carries some load from the shared nodes. From the classical shear-lag model (Hull & Clyne, 1996), increasing the diameter of the inclusions leads to a fall in the normal stress of the inclusions. This hence lowered the composite modulus when stress averaging in this study case. Across the curves, the composite modulus also increases from short to long rods as the aspect ratio of the rods also changes the macroscopic properties (Hull & Clyne, 1996). For ZC1 samples, the average diameter and length of rods are ≈0.5 and 5 μm, respectively, exanimated from several SEM images throughout this work (Fig. S2). Eventually, this leads to a computed composite modulus of 5 GPa, which is very close to the experimental values of 4.76 GPa. Also, the numerical values of stresses in the y-direction (tensile) are shown in Fig. 5d–e. A typical curve in diagram b with zero normal stress at the ends of the rods because of high shear stress at the interfaces from the mismatch of elastic properties. Then, the normal stress monotonically increases up to half length of the rods reaching a peak of 22 MPa. The normal stress in the cross-section of rods becomes more uniform as moving toward the half-length of the rods. Fig. 5e shows the uniform stress distribution across the middle of the entire geometry. In addition, the 3D stress field reveals the complexity of the stress distribution near the ends of the rods.

3.5. Sensing of human physiological motions

CNF-based composite materials have been used for the preparation of flexible device applications (Qin et al., 2008; Qin et al., 2022; Wang et al., 2007; Wang & Song, 2006) and ZnO further added to improve the functional properties. In our work, the beneficial stress-strain stress between CNF layers and ZnO microrods is favorable for piezoelectric sensors. Therefore, the composites were used for sensing human physiological motions, potentially applicable for health monitoring. The CNF sensor has lower sensitivity toward the smaller mechanical deformation and resulted in a poor signal under fist-clenching motions (mounted on the wrist) as shown in Fig. 6a. However, ZC composites show higher sensitivity due to increased piezoelectric responses of the composite due to the presence of ZnO microrods. At higher mechanical deformations e.g. during finger, elbow, or knee bending CNF sensor resulted in good signals, which were again improved for ZnO/CNF sensors. Finger bending could generate 15 mV and 45 mV by using CNF and ZC1 sensors, respectively. Under elbow bending, CNF and ZC1 generated 8 mV and 30 mV, respectively. As for knee bending, the output voltage of CNF and ZC1 were 30 mV and 40 mV. The lower difference in the performances at higher mechanical deformations is due to the reduced local deformations at the higher overall deformation. With the increased ZnO content the piezoelectric output remains almost constant due to the reduced mechanical properties and flexibility of the composite films (Fig. S3). Additionally, the output voltages from these ZnO/CNF composite sensors were similar to or higher than the previous reports (Table S4).

4. Conclusion

Herein, we report *in situ* preparation of ZnO/CNF layered composites, where ZnO microrods are sandwiched between CNF layers. Highly charged CNF act as a nucleating agent for ZnO growth and serve as a supporting matrix for the ZnO microrods. DIC studies confirm that a homogenous distribution of the ZnO microrods is achieved in the ZC1 composite without ultrasonication. Further, the computational homogenization predicts that the CNF coating on the ZnO microrods acts as a stress transfer bridge, which confirms our hypothesis. The normal stress in the rod is homogenously concentrated across the rod diameter (cross section) and it is higher in the middle of the length of the rod (on the rod surface). The composite modulus calculated from the idealized periodic structure is similar to the experimental values for the low Zn content film suggesting the accuracy of the employed computational

homogenization model. However, issues such as the uneven distribution of rods may be a limiting factor and a non-periodic geometry also deserves further development. Further, with a variation of Zn ion concentration, ZnO crystallite size and loading in the composite increased with increased concentration without changing the ZnO microrods morphology. Composite with lower ZnO loading (32.9 wt%) shows smaller strain fluctuation and better mechanical strength. The efficient stress transfer between CNF and ZnO allows efficient physiological motion sensing, potentially applicable for human health monitoring.

CRediT authorship contribution statement

Ying Gao: Methodology, Investigation, Validation, Data curation, Data, Formal analysis, Writing - original draft. **Bin Chen**: Data, Formal analysis. **Marcus Vinícius Tavares da Costa**: Data, Formal analysis. **Hongqi Dai**: Writing – review & editing. **Farsa Ram**: Conceptualization, Investigation, Data curation, Writing – review & editing and supervising. **Yuanyuan Li**: Conceptualization, Writing – review & editing and supervising.

Declaration of competing interest

The authors declare that they have no known competing financial interests or personal relationships that could have appeared to influence the work reported in this paper.

Data availability

Data will be made available on request.

Acknowledgments

We acknowledge the funding from Vetenskapsrådet (VR, No. 2017-05349), Knut & Alice foundation via the Wallenberg Wood Science Center, and European Research Council (ERC) under the European Union's Horizon 2020 research and innovation programme (No. 742733). Ying acknowledges financial support from project funded by the National First-class Disciplines (PNFD) and the Priority Academic Program Development of Jiangsu Higher Education Institutions (PAPD). Special thanks to Lars Berglund for supporting the work. Erfan Oliaei is acknowledged for preparing the CNF samples. Xiaoying Xu is acknowledged for taking photos of samples. Lengwan Li is acknowledged for testing the zeta potential, charge density and AFM.

Appendix A. Supplementary data

Supplementary data to this article can be found online at https://doi.org/10.1016/j.carbpol.2022.120536.

References

Chen, H., Xing, J., Xi, J., Pu, T., Liu, H., & Zhu, J. (2021). Origin of high piezoelectricity in low-temperature sintering PZT-based relaxor ferroelectric ceramics. *Journal of Alloys and Compounds, 860*, Article 157930.

Dehghani, M., Nadeem, H., Singh Raghuwanshi, V., Mahdavi, H., Banaszak Holl, M. M., & Batchelor, W. (2020). ZnO/cellulose nanofiber composites for sustainable sunlight-driven dye degradation. *ACS Applied Nano Materials, 3*(10), 10284–10295.

Ding, C., Cai, C., Yin, L., Wu, Q., Pan, M., & Mei, C. (2019). Mechanically adaptive nanocomposites with cellulose nanocrystals: Strain-field mapping with digital image correlation. *Carbohydrate Polymers, 211*, 11–21.

Fu, F., Gu, J., Xu, X., Xiong, Q., Zhang, Y., Liu, X., & Zhou, J. (2017). Interfacial assembly of ZnO–cellulose nanocomposite films via a solution process: A one-step biomimetic approach and excellent photocatalytic properties. *Cellulose, 24*(1), 147–162.

Gao, P. X., Song, J., Liu, J., & Wang, Z. L. (2007). Nanowire piezoelectric nanogenerators on plastic substrates as flexible power sources for nanodevices. *Advanced Materials, 19*(1), 67–72.

Gerbreders, V., Krasovska, M., Sledevskis, E., Gerbreders, A., Mihailova, I., Tamanis, E., & Ogurcovs, A. (2020). Hydrothermal synthesis of ZnO nanostructures with controllable morphology change. *CrystEngComm, 22*(8), 1346–1358.

Gullapalli, H., Vemuru, V. S. M., Kumar, A., Botello-Mendez, A., Vajtai, R., Terrones, M., Nagarajaiah, S., & Ajayan, P. M. (2010). Flexible piezoelectric zno-paper nanocomposite strain sensor. *Small, 6*(15), 1641–1646.

Hoogendoorn, B. W., Birdsong, B. K., Capezza, A. J., Ström, V., Li, Y., Xiao, X., & Olsson, R. T. (2022). Ultra-low concentration of cellulose nanofibers (CNFs) for enhanced nucleation and yield of ZnO nanoparticles. *Langmuir, 38*(41), 12480–12490.

Hull, D., & Clyne, T. (1996). 8- Strength of composites. In (2nd ed.,*Cambridge Solid State Science SeriesAn introduction to composite materials* (pp. 158–207). Cambridge: Cambridge University Press.

Karakoç, A., Miettinen, A., Virkajärvi, J., & Joffe, R. (2021). Effective elastic properties of biocomposites using 3D computational homogenization and X-ray microcomputed tomography. *Composite Structures, 273*, Article 114302.

Karlsson, M. E., Mamie, Y. C., Calamida, A., Gardner, J. M., Ström, V., Pourrahimi, A. M., & Olsson, R. T. (2018). Synthesis of zinc oxide nanorods via the formation of sea urchin structures and their photoluminescence after heat treatment. *Langmuir, 34*(17), 5079–5087.

Kobayashi, Y., Saito, T., & Isogai, A. (2014). Aerogels with 3D ordered nanofiber skeletons of liquid-crystalline nanocellulose derivatives as tough and transparent insulators. *Angewandte Chemie, 126*(39), 10562–10565.

Kumar, A., & Dixit, C. K. (2017). 3 - methods for characterization of nanoparticles. In S. Nimesh, R. Chandra, & N. Gupta (Eds.), *Advances in nanomedicine for the delivery of therapeutic nucleic acids* (pp. 43–58). Woodhead Publishing.

Li, Y., Sun, H., Zhang, Y., Xu, M., & Shi, S. Q. (2019). The three-dimensional heterostructure synthesis of ZnO/cellulosic fibers and its application for rubber composites. *Composites Science and Technology, 177*, 10–17.

Li, X., Zhang, L., Wang, Z., Wu, S., & Ma, J. (2021). Cellulose controlled zinc oxide nanoparticles with adjustable morphology and their photocatalytic performances. *Carbohydrate Polymers, 259*, Article 117752.

Li, Z., Han, X., Li, Y., & Chan, H. L. W. (2021). Fabrication and properties of NaNbO3 sintered by two-step method. *Applied Physics A, 127*(5), 1–7.

Liao, Q., Zhang, Z., Zhang, X., Mohr, M., Zhang, Y., & Fecht, H. J. (2014). Flexible piezoelectric nanogenerators based on a fiber/ZnO nanowires/paper hybrid structure for energy harvesting. *Nano Research, 7*(6), 917–928.

Lizundia, E., Urruchi, A., Vilas, J. L., & León, L. M. (2016). Increased functional properties and thermal stability of flexible cellulose nanocrystal/ZnO films. *Carbohydrate Polymers, 136*, 250–258.

Ltaief, S., Jabli, M., & Abdessalem, S. B. (2021). Immobilization of copper oxide nanoparticles onto chitosan biopolymer: Application to the oxidative degradation of naphthol blue black. *Carbohydrate Polymers, 261*, Article 117908.

Luo, Z., Liu, J., Lin, H., Ren, X., Tian, H., Liang, Y., Wang, W., Wang, Y., Yin, M., Huang, Y., & Zhang, J. (2020). In situ fabrication of nano zno/bcm biocomposite based on ma modified bacterial cellulose membrane for antibacterial and wound healing. *International Journal of Nanomedicine, 15*, 1–15.

Mirkhalaf, S. M., Eggels, E. H., van Beurden, T. J. H., Larsson, F., & Fagerström, M. (2020). A finite element based orientation averaging method for predicting elastic properties of short fiber reinforced composites. *Composites Part B: Engineering, 202*, Article 108388.

Molnár, G., Rodney, D., Martoïa, F., Dumont, P. J. J., Nishiyama, Y., Mazeau, K., & Orgéas, L. (2018). Cellulose crystals plastify by localized shear. *Proceedings of the National Academy of Sciences of the United States of America, 115*(28), 7260–7265.

Nakamura, K. I., Wada, M., Kuga, S., & Okano, T. (2004). Poisson's ratio of cellulose Iβ and cellulose II. *Journal of Polymer Science Part B: Polymer Physics, 42*(7), 1206–1211.

Nie, S., Zhang, Y., Wang, L., Wu, Q., & Wang, S. (2019). Preparation and characterization of nanocomposite films containing nano-aluminum nitride and cellulose nanofibrils. *Nanomaterials, 9*(8), 1121.

Ong, C. B., Ng, L. Y., & Mohammad, A. W. (2018). A review of ZnO nanoparticles as solar photocatalysts: Synthesis, mechanisms and applications. *Renewable and Sustainable Energy Reviews, 81*, 536–551.

Pan, B., Qian, K., Xie, H., & Asundi, A. (2009). Two-dimensional digital image correlation for in-plane displacement and strain measurement: A review. *Measurement Science and Technology, 20*(6), Article 062001.

Park, T., Kim, N., Kim, D., Kim, S. W., Oh, Y., Yoo, J. K., You, J., & Um, M. K. (2019). An organic/inorganic nanocomposite of cellulose nanofibers and ZnO nanorods for highly sensitive, reliable, wireless, and wearable multifunctional sensor applications. *ACS Applied Materials and Interfaces, 11*(51), 48239–48248.

Qin, Y., Wang, X., & Wang, Z. L. (2008). Microfibre-nanowire hybrid structure for energy scavenging. *Nature, 451*(7180), 809–813.

Qin, Y., Mo, J., Liu, Y., Zhang, S., Wang, J., Fu, Q., Wang, S., & Nie, S. (2022). Stretchable triboelectric self-powered sweat sensor fabricated from self-healing nanocellulose hydrogels. *Advanced Functional Materials, 32*, 22–1846.

Rabani, I., Lee, S. H., Kim, H. S., Yoo, J., Hussain, S., Maqbool, T., & Seo, Y. S. (2021). Engineering-safer-by design ZnO nanoparticles incorporated cellulose nanofiber hybrid for high UV protection and low photocatalytic activity with mechanism. *Journal of Environmental Chemical Engineering, 9*(5), Article 105845.

Ram, F., Suresh, K., Torris, A., Kumaraswamy, G., & Shanmuganathan, K. (2021). Highly compressible ceramic/polymer aerogel-based piezoelectric nanogenerators with enhanced mechanical energy harvesting property. *Ceramics International, 47*(11), 15750–15758.

Ram, F., Garemark, J., Li, Y., & Berglund, L. (2022). Scalable, efficient piezoelectric wood nanogenerators enabled by wood/ZnO nanocomposites. *Composites Part A: Applied Science and Manufacturing, 160*, Article 107057.

Sada, T., Tsuji, K., Ndayishimiye, A., Fan, Z., Fujioka, Y., & Randall, C. A. (2021). High permittivity BaTiO3 and BaTiO3-polymer nanocomposites enabled by cold sintering with a new transient chemistry: Ba(OH)2•8H2O. *Journal of the European Ceramic Society, 41*(1), 409–417.

Sarkar, S., Guibal, E., Quignard, F., & SenGupta, A. K. (2012). Polymer-supported metals and metal oxide nanoparticles: Synthesis, characterization, and applications. *Journal of Nanoparticle Research, 14*(2), 1–24.

Schreier, H., Orteu, J. J., & Sutton, M. A. (2009). In *Image correlation for shape, motion and deformation measurements: Basic concepts, theory and applications* (Vol. 1, pp. 1–12). Boston, MA: Springer-Verlag, US.

Serrano, A., Caballero-Calero, O., García, M.Á., Lazić, S., Carmona, N., Castro, G. R., Martín-González, M., & Fernández, J. F. (2020). Cold sintering process of ZnO ceramics: Effect of the nanoparticle/microparticle ratio. *Journal of the European Ceramic Society, 40*(15), 5535–5542.

Shifrina, Z. B., Matveeva, V. G., & Bronstein, L. M. (2020). Role of polymer structures in catalysis by transition metal and metal oxide nanoparticle composites. *Chemical Reviews, 120*(2), 1350–1396.

Siponkoski, T., Nelo, M., Ilonen, N., Juuti, J., & Jantunen, H. (2022). High performance piezoelectric composite fabricated at ultra low temperature. *Composites Part B: Engineering, 229*, Article 109486.

Song, G., Lancelon-Pin, C., Chen, P., Yu, J., Zhang, J., Su, L., Wada, M., Kimura, T., & Nishiyama, Y. (2021). Time-dependent elastic tensor of cellulose nanocrystal probed by hydrostatic pressure and uniaxial stretching. *Journal of Physical Chemistry Letters, 12*(15), 3779–3785.

Ul-Islam, M., Khattak, W. A., Ullah, M. W., Khan, S., & Park, J. K. (2014). Synthesis of regenerated bacterial cellulose-zinc oxide nanocomposite films for biomedical applications. *Cellulose, 21*(1), 433–447.

Wang, Z. (2004). Nanostructures of zinc oxide. *Materials Today, 7*(6), 26–33.

Wang, Z. L., & Song, J. (2006). Piezoelectric nanogenerators based on zinc oxide nanowire arrays. *Science, 312*(5771), 242–246.

Wang, X., Song, J. J., & Wang, Z. (2007). Direct-current nanogenerator driven by ultrasonic waves. *Science, 316*(5821), 102–105.

Wang, B., Benitez, A. J., Lossada, F., Merindol, R., & Walther, A. (2016). Bioinspired mechanical gradients in cellulose nanofibril/polymer nanopapers. *Angewandte Chemie, 128*(20), 6070–6074.

Wang, F., Wang, H., Yang, Q., Zhang, Z., & Yan, K. (2021). Fine-grained relaxor ferroelectric PMN-PT ceramics prepared using hot-press sintering method. *Ceramics International, 47*(11), 15005–15009.

Wang, Z., Bockstaller, M. R., & Matyjaszewski, K. (2021). Synthesis and applications of ZnO/polymer nanohybrids. *ACS Materials Letters, 3*(5), 599–621.

Wu, R., Qian, H., & Zhang, D. (2016). Robust full-field measurement considering rotation using digital image correlation. *Measurement Science and Technology, 27*(10), Article 105002.

Yan, X., Dickinson, M., Schirer, J. P., Zou, C., & Gao, W. (2010). Face dependence of mechanical properties of a single ZnO nano/microrod. *Journal of Applied Physics, 108*(5), Article 056101.

Yvonnet, J. (2019). In *Computational homogenization of heterogeneous materials with finite elements* (Vol. 258, pp. 161–209). Springer International Publishing.

Zhang, Y., Ge, L., Li, M., Yan, M., Ge, S., Yu, J., Song, X., & Cao, B. (2014). Flexible paper-based ZnO nanorod light-emitting diodes induced multiplexed photoelectrochemical immunoassay. *Chemical Communications, 50*(12), 1417–1419.

Zhang, K., Tao, P., Zhang, Y., Liao, X., & Nie, S. (2019). Highly thermal conductivity of CNF/AlN hybrid films for thermal management of flexible energy storage devices. *Carbohydrate Polymers, 213*, 228–235.